The Cryosphere Discuss., 9, 5445–5483, 2015
www.the-cryosphere-discuss.net/9/5445/2015/
doi:10.5194/tcd-9-5445-2015

The Cryosphere Discussions
Open Access

Retrieval of the thickness of undeformed sea ice from C-band compact polarimetric SAR images

X. Zhang[1], W. Dierking[2], J. Zhang[1], J. M. Meng[1], and H. T. Lang[3]

[1]First Institute of Oceanography, State Oceanic Administration, Qingdao, China
[2]Alfred Wegener Institute for Polar and Marine Research, Bremerhaven, Germany
[3]Beijing University of Chemical Technology, Beijing, China

Received: 29 August 2015 – Accepted: 30 September 2015 – Published: 15 October 2015

Correspondence to: X. Zhang (schuman.zhang@gmail.com)

Published by Copernicus Publications on behalf of the European Geosciences Union.

Abstract

In this paper we introduce a parameter for the retrieval of the thickness of undeformed first-year sea ice that is specifically adapted to compact polarimetric SAR images. The parameter is denoted as "CP-Ratio". In model simulations we investigated the sensitivity of CP-Ratio to the dielectric constant, thickness, surface roughness, and incidence angle. From the results of the simulations we deduced optimal conditions for the thickness retrieval. On the basis of C-band CTLR SAR data, which were generated from Radarsat-2 quad-polarization images acquired jointly with helicopter-borne sea ice thickness measurements in the region of the Sea of Labrador, we tested empirical equations for thickness retrieval. An exponential fit between CP-Ratio and ice thickness provides the most reliable results. Based on a validation using other compact polarimetric SAR images from the same region we found a root mean square (rms) error of 8 cm and a maximum correlation coefficient of 0.92 for the retrieval procedure when applying it on level ice of 0.9 m mean thickness.

1 Introduction

The knowledge of the ice thickness distribution is essential in order to understand the dynamics and thermodynamics of the Arctic and Antarctic sea ice. For example, estimates of sea ice thickness are important for the determination of spatial variations of ice strength and mass (Soulis et al., 1989). The thickness of first-year and multi-year ice affects the salt and freshwater exchange between ice and ocean (Vancoppenolle et al., 2005).

To date, sea ice thickness can be measurement by upward-looking sonars moored on the ocean floor (Wadhams, 1980) or by electromagnetic induction sounders mounted on helicopters or ships (Goebell, 2011; Haas et al., 1997). Although these methods provide data with sufficient accuracy, they are time consuming and/or have poor spatial coverage. Low-frequency microwave radiometers, for example the L-band

TCD
9, 5445–5483, 2015

SMOS (Soil Moisture and Ocean Salinity mission) radiometer, receive signal contributions from larger penetration depths in sea ice and thus contain information on the ice thickness (Kaleschke et al., 2012; Huntemann et al., 2014). However, the sea ice products derived from such radiometers only focus on large-scale spatial and temporal variations (Kwok et al., 2009), and their coarse resolution prevents the retrieval of the sea ice thickness distribution on a finer scale. This situation encouraged us to study alternative approaches to obtain sea-ice thickness distributions at much higher spatial resolution. Synthetic aperture radar (SAR) can provide observations all-day and at almost all-weather conditions at high spatial resolution. Hence, SAR is in general very useful for different mapping tasks. Recent papers have demonstrated the feasibility of retrieving ice thickness from SAR data (Wakabayashi et al., 2004; Nakamura et al., 2009; Toyota et al., 2009; Liu et al., 2013; Kim et al., 2012). A number of studies have shown that the co-polarized ratio (Wakabayashi et al., 2004; Nakamura et al., 2009; Toyota et al., 2009) and the alpha angle (Liu et al., 2013) reveal good correlations with the thickness of first-year level ice. The good correlations were attributed to the fact that the co-polarized ratio and the alpha values are sensitive to the dielectric constants of the ice surface layer which changes due to the process of desalination during ice growth. The relationship between relatively thick ice, on the one hand, and co-polarized correlation and cross-polarized ratio, on the other hand, was also investigated for multi-year ice (MYI) areas in the Arctic Sea (Kim et al., 2012). It was found that the degree of depolarization is linked to the thickness of the older ice as ice surface roughness increases and salinity decreases. In conclusion, we anticipate the potential for estimating sea-ice thickness from polarimetric SAR imagery under certain conditions.

The major limitation of the available quad- and dual-polarization SAR data is the reduced swath width that makes those imaging modes less appropriate for routine mapping, which requires large-scale coverage. The quad-polarization mode on Radarsat-2, for example, has only a swath width of 25 km. The swath width of the VV/HH dual-polarization Stripmap mode on TerraSAR-X is 15 km. Compact polarimetry (CP) SAR modes have a greater amount of polarization information than dual-polarization

TCD
9, 5445–5483, 2015

modes, while covering much greater swath widths compared to quad-polarization modes (Souyris et al., 2005; Raney, 2007). Considering that CP data will be available for swath widths of 350 km and spatial resolutions of 50 m (Salberg et al., 2014), the application of CP is a key issue for sea ice surveillance, making it is well suited for operational sea ice monitoring. One apparent disadvantage of the CP mode as compared to dual- or quad-polarization mode is the fact that the HH, VV, and HV signal combinations are not directly measured. This means that the co-polarized ratio (Wakabayashi et al., 2004; Nakamura et al., 2009; Toyota et al., 2009) and the cross-polarized ratio (Kim et al., 2012) which are often used as an ice thickness proxy cannot be directly calculated in CP mode. Although CP SAR images have been used to distinguish sea ice types (Dabboor and Geldsetzer, 2014; Charbonneau et al., 2010), to our knowledge there have been no published studies on its use for ice-thickness detection in the open literature until now. Therefore, in this study, we focus on the directly retrieval of sea ice thickness from CP SAR data.

There are three CP configurations (Nord et al., 2009). The first architecture is the $\pi/4$ mode assuming a slant linear transmission and horizontal (H) and vertical (V) receptions (Souyris et al., 2005). The second is the dual circular (DC) mode operating a single circular polarization transmission and two orthogonal circular polarizations on reception. The last approach is circular transmission and H and V receptions (called CTLR mode). Among these three compact polarization modes, the latter has been ranked to be the most promising in terms of performance and receiver complexity (Denbina and Collins, 2012; Panigrahi et al., 2012; Salberg et al., 2014). The Mini-SAR on Chandraayan-1, the first practical radar, is based on the CTLR architecture. The current Indian RISAT-1, the Japanese ALOS-2 and the planned Canadian Radarsat Constellation Mission also support the CTLR mode (Salberg et al., 2014).

In this study, we considered the CTLR mode and developed an approach to directly retrieve the thickness of undeformed first-year sea-ice from CP SAR data. The paper is organized as follows: in Sect. 2 we introduce a new parameter to estimate ice-thickness and demonstrate its sensitivity to different ice parameters by numerical modeling in

TCD
9, 5445–5483, 2015

Sect. 3. In Sect. 4, an empirical relationship based on a comparison of CP-SAR signatures with ice thickness data obtained from electromagnetic induction sounding is presented, and the retrieval performance of this algorithm is described. Further discussions and conclusion are presented in Sect. 5.

2 Model and method

2.1 Full polarimetry and compact polarimetry

The full polarimetric radar scattering return can be represented by the scattering matrix **S**

$$\mathbf{S} = \begin{bmatrix} S_{\mathrm{HH}} & S_{\mathrm{HV}} \\ S_{\mathrm{HV}} & S_{\mathrm{VV}} \end{bmatrix}. \tag{1}$$

We use the coherence matrix **T** to evaluate the second-order statistics of the scattering matrix **S**. The coherence matrix **T** formed from the elements of the scattering matrix **S** is

$$\mathbf{T} = \frac{1}{2}\begin{bmatrix} \left\langle |S_{\mathrm{HH}} + S_{\mathrm{VV}}|^2 \right\rangle & \langle (S_{\mathrm{HH}} + S_{\mathrm{VV}})(S_{\mathrm{HH}} - S_{\mathrm{VV}})^* \rangle & 2\langle (S_{\mathrm{HH}} + S_{\mathrm{VV}})S_{\mathrm{HV}}^* \rangle \\ \langle (S_{\mathrm{HH}} - S_{\mathrm{VV}})(S_{\mathrm{HH}} + S_{\mathrm{VV}})^* \rangle & \left\langle |S_{\mathrm{HH}} - S_{\mathrm{VV}}|^2 \right\rangle & 2\langle (S_{\mathrm{HH}} - S_{\mathrm{VV}})S_{\mathrm{HV}}^* \rangle \\ 2\langle S_{\mathrm{HV}}(S_{\mathrm{HH}} + S_{\mathrm{VV}})^* \rangle & 2\langle S_{\mathrm{HV}}(S_{\mathrm{HH}} - S_{\mathrm{VV}})^* \rangle & 4\left\langle |S_{\mathrm{HV}}|^2 \right\rangle \end{bmatrix} \tag{2}$$

where * denotes the complex conjugate and $< \cdot >$ the ensemble average.

Consider the CTLR mode suggested by Raney (2007) with right circular polarization on transmission and an orthogonal combination of H and V polarizations on receiption. The scattering vectors for the CTLR mode are given by

$$\boldsymbol{k}_{\mathrm{CTLR}} = [S_{\mathrm{RH}} S_{\mathrm{RV}}]^T = [S_{\mathrm{HH}} - iS_{\mathrm{HV}} - iS_{\mathrm{VV}} + S_{\mathrm{HV}}]^T \Big/ \sqrt{2}. \tag{3}$$

TCD
9, 5445–5483, 2015

We set

$$\Sigma_H = S_{RH} + iS_{RV} \quad \Sigma_V = S_{RH} - iS_{RV}. \tag{4}$$

From Eq. (3), it follows that

$$\Sigma_H = S_{HH} + S_{VV} \quad \Sigma_V = S_{HH} - S_{VV} - i2S_{HV}. \tag{5}$$

The terms $\left\langle |\Sigma_h|^2 \right\rangle$ and $\left\langle |\Sigma_V|^2 \right\rangle$ can be expressed as

$$\begin{aligned}
\left\langle |\Sigma_h|^2 \right\rangle &= \langle (S_{HH} + S_{VV})(S_{HH} + S_{VV})^* \rangle \\
&= \left\langle |S_{HH} + S_{VV}|^2 \right\rangle, \\
\left\langle |\Sigma_V|^2 \right\rangle &= \langle (S_{HH} - S_{VV} - i2S_{HV})(S_{HH} - S_{VV} - i2S_{HV})^* \rangle \\
&= \langle (S_{HH} - S_{VV})(S_{HH} - S_{VV})^* \rangle + \left\langle i2S_{HV}^*(S_{HH} - S_{VV}) \right\rangle \\
&\quad - \langle i2S_{HV}(S_{HH} - S_{VV})^* \rangle + 4|S_{HV}|^2 \\
&= \left\langle |S_{HH} - S_{VV}|^2 \right\rangle + \left\langle i2S_{HV}^*(S_{HH} - S_{VV}) \right\rangle - \langle i2S_{HV}(S_{HH} - S_{VV})^* \rangle + 4|S_{HV}|^2.
\end{aligned} \tag{6}$$

Under the assumption of reflection symmetry the cross- and co-polarized scattering coefficients are uncorrelated. This assumption is reasonable for snow and sea ice surfaces at various frequencies and for different spatial scales (Souyris et al., 2005). Hence

$$\langle S_{HV}^* S_{VV} \rangle = \langle S_{HH} S_{HV}^* \rangle \approx 0. \tag{7}$$

and Eq. (6) can be rewritten by the elements of coherence matrix **T**:

$$\left\langle |\Sigma_h|^2 \right\rangle = \left\langle |S_{HH} + S_{VV}|^2 \right\rangle = t_{11} \quad \left\langle |\Sigma_V|^2 \right\rangle = \left\langle |S_{HH} - S_{VV}|^2 \right\rangle + 4|S_{HV}|^2 = t_{22} + t_{33}. \tag{8}$$

TCD
9, 5445–5483, 2015

2.2 X-Bragg model and X-SPM model

For explaining the surface scattering characteristics from smooth level sea ice the small perturbation method (SPM) can be applied for the typical ranges of RMS height and correlation lengths found for this type of ice. By doing so the underlying assumption is that the received radar signatures are typical for Bragg scattering. However the SPM fails to describe cross-polarization and de-polarization effects usually observed in real SAR data. In order to overcome these limitations and to widen the SPM range of validity, an extended Bragg model (termed X-Bragg model) was presented by Hajnsek et al. (2003). In the X-Bragg model the scattering surface is composed of rough randomly tilted facets that are large with respect to the wavelength but small with respect to the spatial resolution of the sensor. Scattering from each rough facet is evaluated by employing the SPM, whereat the facet random tilt causes both a random variation $\Delta\theta$ of the incident angle θ and a random rotation β of the local incidence plane around the line of sight. In the X-Bragg model, the random incidence angle variation $\Delta\theta$ is ignored, and the incidence plane angle of rotation β is assumed to be uniformly distributed in an interval $(-\beta_1, \beta_1)$, where the parameter β_1 is used to characterize the large-scale roughness (Monaco et al., 2009).

In order to improve the range of validity of the X-Bragg model, different approaches (termed X-SPM model) were proposed by Monaco et al. (2009) and Iodice et al. (2011). In those studies, more realistic distributions of β and $\Delta\theta$ were derived by assuming that the range and azimuth facet slopes are Gaussian random variables. The coherency matrix of the X-SPM model ($\mathbf{T}_{\text{X-SPM}}$) after ensemble averaging over the local incident angle θ_I and rotation angle β can be expressed as follows (Monaco et al., 2009)

TCD
9, 5445–5483, 2015

$$\mathbf{T}_{\text{X-SPM}} = \rho \begin{bmatrix} \left\langle |R_S + R_P|^2 \right\rangle_{|\theta_l} & c_2\langle (R_S - R_P)(R_S + R_P)^* \rangle_{|\theta_l} & 0 \\ c_2\langle (R_S + R_P)(R_P - R_S)^* \rangle_{|\theta_l} & cc_2 \left\langle |R_S - R_P|^2 \right\rangle_{|\theta_l} & 0 \\ 0 & 0 & ss_2 \left\langle |R_S - R_P|^2 \right\rangle_{|\theta_l} \end{bmatrix}, \quad (9)$$

$$cc = \left\langle \cos^2\beta \right\rangle_{|\beta} = \sqrt{\frac{\pi \sin^2\theta}{2\sigma^2}} \exp\left\{\frac{\sin^2\theta}{2\sigma^2}\right\} \text{ Erfc}\left\{\sqrt{\frac{\sin^2\theta}{2\sigma^2}}\right\},$$

$$c_2 = \langle \cos 2\beta \rangle_{|\beta} = -1 + 2cc,$$

$$cc_2 = \left\langle \cos^2 2\beta \right\rangle_{|\beta} = \frac{\sin^2\theta}{\sigma^2} + (1 - 2cc)\frac{\sin^2\theta + \sigma^2}{\sigma^2},$$

$$ss_2 = \left\langle \sin^2 2\beta \right\rangle_{|\beta} = 1 - cc_2.$$

$\langle\rangle_{\theta_l}$ means averaging over the local incidence angle θ_l which is used to characterize random slope variations of the facets; $\langle\rangle_{|\beta}$ means averaging over the rotation angle β; ρ includes small scale roughness effects, and σ is the standard deviation of surface slope which is a Gaussian random variable. R_P and R_S are the Bragg scattering coefficients perpendicular and parallel to the incident plane, respectively. Both are functions of the complex permittivity ε and the incident angle θ

$$R_S = \frac{\cos\theta - \sqrt{\varepsilon - \sin^2\theta}}{\cos\theta + \sqrt{\varepsilon - \sin^2\theta}} \quad R_P = \frac{(\varepsilon - 1)\left[\sin^2\theta - \varepsilon(1 + \sin^2\theta)\right]}{(\varepsilon\cos\theta + \sqrt{\varepsilon - \sin^2\theta})^2}. \quad (10)$$

In the paper by Monaco et al. (2009) it is demonstrated that the X-SPM model coincides with the X-Bragg model when the standard deviation of the surface slope is zero, and that the X-Bragg model can only be applied for standard deviations of the surface slope $\sigma < 0.1$. When $\sigma > 0.1$, the effects of incidence angle fluctuations, which is ignored in

TCD
9, 5445–5483, 2015

the X-Bragg model, is significant (Monaco et al., 2009). Because of its wider range of validity, we used the X-SPM model in our study.

2.3 Inversion model

For ice thickness retrievals we propose the ratio between $\left\langle |\Sigma_V|^2 \right\rangle$ and $\left\langle |\Sigma_H|^2 \right\rangle$ (here called CP-Ratio). The CP-Ratio can be written as (see Eq. 4)

$$\text{Ratio} = \frac{\left\langle |\Sigma_V|^2 \right\rangle}{\left\langle |\Sigma_H|^2 \right\rangle} = \frac{\left\langle |S_{RH} - iS_{RV}|^2 \right\rangle}{\left\langle |S_{RH} + iS_{RV}|^2 \right\rangle}. \tag{11}$$

By relating the CP-Ratio to the elements of the coherency matrix given for the X-SPM we obtain

$$\text{Ratio} = \frac{\left\langle |\Sigma_V|^2 \right\rangle}{\left\langle |\Sigma_H|^2 \right\rangle} = \frac{cc_2 \left\langle |R_S - R_P|^2 \right\rangle_{|\theta_I} + ss_2 \left\langle |R_S - R_P|^2 \right\rangle_{|\theta_I}}{\left\langle |R_S + R_P|^2 \right\rangle_{|\theta_I}} = \frac{\left\langle |R_S - R_P|^2 \right\rangle_{|\theta_I}}{\left\langle |R_S + R_P|^2 \right\rangle_{|\theta_I}}. \tag{12}$$

Equation (12) shows that the CP-Ratio is controlled by ensemble averages of the difference and sum of the Bragg coefficients with respect to the incidence angle. From Monaco et al. (2009), the probability density function for $\cos\theta_I$ is a normal distribution with mean $\cos\theta$ and standard deviation equal to $\sigma \sin\theta$. After averaging over variations of the local incidence angle θ_I, the CP-Ratio is dependent on the dielectric constant of surface ε, the incidence angle θ, and the standard deviation of surface slope σ.

We calculated the CP-Ratio as a function of the standard deviation of surface slope σ assuming $\varepsilon = 3$ (Fig. 1). The results show that the CP-Ratio increases with increasing standard deviation of the surface slope at fixed incidence angles and with increasing incidence angle at fixed σ. The relationship between CP-Ratio and the dielectric constant is presented in Fig. 2. When the incidence angle is constant, the CP-Ratio reveals monotonically increasing values with increasing dielectric constant.

TCD
9, 5445–5483, 2015

With respect to our simulated results shown in Figs. 1 and 2, it is important to note that the proposed parameter CP-Ratio is sensitive to the variation of the dielectric constant and almost insensitive to the surface slope variations if $\sigma < 0.15$. Hence it is well-suited for detecting changes of the dielectric constant of smooth first-year level ice for which Bragg surface scattering is dominant and volume scattering can be neglected in most cases.

Desalination of the ice occurs parallel to the growth of sea ice. The ice salinity decreases by brine drainage while the ice thickness increases (Kovacs, 1996). The desalination process, in turn, causes a decrease of the dielectric constant of the ice. The principle of ice thickness detection is to relate changes of the dielectric constant to ice thickness growth.

3 A simulation study

3.1 Forward scattering model

In this section, we describe the combined use of an ice growth model and an electromagnetic scattering model for level sea ice to study sensitivities of CP-Ratio to different ice and radar properties. We applied the scattering model proposed by Nghiem et al. (1995) to simulate the sea ice volume scattering and absorption by brine inclusions. The surface contribution was calculated with the polarimetric two-scale model (PTSM) (Iodice et al., 2011, 2013) and incoherently added to the volume term.

The sea ice scattering model configuration is presented in Fig. 3. The uppermost layer is air with permittivity ε_0, the lowermost medium is seawater with complex permittivity ε_2, both enclosing the ice layer. The ice surface roughness is described by the correlation length l, rms height s, and the standard deviation of the surface slope variation σ. The thickness and surface temperature of the sea ice layer are T_0 and H. The sea ice background is assumed to be pure ice with complex permittivity ε_i. The complex permittivity of brine inclusions is ε_b, and their fractional volume is f_v. The rela-

TCD
9, 5445–5483, 2015

tive permittivity of the sea ice ε_{eff} is a function of the volume fraction of brine inclusions (Arcone et al., 1986; Vant et al., 1978). Thickness and permittivity of sea ice are subject to dynamic changes during the ice growth process. The small-scale surface roughness (on cm-scale) may also change over time (e.g. frost flower growth). Here we do not consider deformation processes causing surface roughness components on the order of meters.

For ice growth simulations we use a 1-D thermodynamic model developed by Maykut (1978, 1982) based on the energy balance equations at the atmosphere–ocean boundary. The balance of the heat fluxes at the upper surface of the ice can be expressed as:

$$(1-\alpha)F_{\text{r}} - I_0 + F_{\text{L}} - F_{\text{E}} + F_{\text{S}} + F_{\text{e}} + F_{\text{C}} = 0 \tag{13}$$

where F_{r} is the incident short wave radiation, αF_{r} is the short wave radiation reflected by ice, and α is the albedo. F_{L} is the incoming long wave radiation, I_0 is the amount of shortwave radiation absorbed in the interior of the ice layer, F_{E} is the long wave radiation emitted by the ice, F_{S} is the sensible heat flux, and F_{e} is the latent heat flux. The last term F_{C} is the upward conductive heat flux, that is the heat from the bottom interface conducted through the ice to the upper surface. The equations and parameters used in this study are listed in Table 1.

Substituting the equations and parameters listed in Table 1 into the Eq. (13) and using the Newton–Raphson iteration method, the sea ice surface temperature T_0 is obtained. Once T_0 is known, F_{E}, F_{S}, F_{e} and F_{C} can be easily calculated. A linear temperature profile within the sea ice layer is assumed. For volume scattering and absorption calculations we use a mean ice temperature (T) calculated from the melting temperature at the ice–water interface and the ice surface temperature. Furthermore, the thickness H (cm), density ρ (Mg m^{-3}), brine volume fraction f_{v}, and permittivity ε_{eff} of sea ice, which are directly related to the volume scattering and absorption in the ice, are obtained by the equations given in Table 2. Lastly the ice surface roughness

TCD
9, 5445–5483, 2015

parameters s, l and σ are set to different values considering the validity range of the X-SPM model (Ulaby et al., 1982; Monaco et al., 2009; Iodice et al., 2011).

3.2 Simulation results

To assess theoretical possibilities and limitations of ice-thickness measurements by CP-Ratio, we simulated the evolution of ice growth for given temperature and wind conditions based on the growth model described in Sect. 3.1. The air temperature and wind speed were set to −15 °C and 10.5 m s^{-1}, respectively, throughout this simulation. The simulation started at an initial ice thickness of 1.0 cm. A finite difference scheme was used to calculate the increase of ice thickness at every 1 h step. After executing about 23 days simulation, the following parameters were extracted as a function of time to drive the sea ice scattering model: ice permittivity ε_{eff}, thickness of ice layer h, and volume fraction of brine inclusions f_{v}. For evaluating the rough surface scattering contribution, the rms height was set to 0.9, 1.4 and 1.8 mm (ks = 0.1, 0.15, and 0.2 for the radar frequency of 5.3 GHz), the correlation length was fixed at 18 mm (kl = 2.0), and the standard deviation of the large-scale slope σ is ranging from 0.05 up to 0.4.

Figure 4 illustrates the simulated sea ice thickness as a function of time, and ice temperature, and volume fraction of brine inclusions as functions of ice thickness. Figure 4 clearly shows that the volume fraction of brine inclusions reduces as ice thickness increases due to the desalination process.

To investigate the dependence of CP-Ratio on the radar incidence angle and ice thickness, the complex scattering coefficients (S_{HH}, S_{VV}, and S_{HV}) were computed for C band (5.3 GHz) at incidence angles of 20–60°. Then the CP-Ratio was calculated from Eq. (12). The relationship between CP-Ratio and sea ice thickness at roughness condition ks = 0.15, kl = 2.0, and σ = 0.1 is shown in Fig. 5. It reveals that CP-Ratio exhibits a monotonically decreasing trend with growing ice-thickness at constant incidence angles as discussed in Sect. 2. It should be noted that the sensitivity of CP-Ratio to vertical ice growth is much higher at smaller ice-thickness values up to approximately 0.4 m. This can be explained by the relationship between salinity and thickness of sea

TCD
9, 5445–5483, 2015

ice. When the sea ice thickness < 0.4 m, the change of salinity is very fast, but for thickness values > 0.4 m, the process of desalination slows down.

Figures 6 and 7 indicate the roughness dependencies of the CP-ratio. In Fig. 6 the standard deviation of the slope parameter σ is varied from 0.05 to 0.4 and the ks and kl values are fixed at 0.15 and 2.0, respectively. When $\sigma < 0.15$ the contribution of the ice-surface slope to the CP-Ratio is small; however, when $\sigma > 0.15$ the contribution of the ice-surface slope becomes significant and weakens the capability of CP-Ratio to estimate thickness. Figure 7 reveals that the small-scale roughness changes in particular the magnitude of the CP-Ratio but its sensitivity to ice thickness remains on acceptable levels, more or less independent of the incidence angle. At larger incidence angles, the magnitude of CP-Ratio is less reduced than at smaller ones. From the results of these simulations, we expect that the proposed new parameter for thickness retrieval has a strong correlation with the thickness of smooth underformed sea ice.

4 Datasets and experimental results

4.1 Field study

On 19–20 March 2011, a field program was conducted by the Canadian Ice Service (CIS) and Fisheries and Oceans Canada along the mid-Labrador coast (Fig. 8) (Prinsenberg et al., 2012). During the field survey, the average air temperature was around -8 to $-12\,^{\circ}$C and the wind speed around 11–15 m s^{-1}. Snow thickness and ice thickness were measured with a helicopter-borne sensor package which consists of a laser altimeter, an electromagnetic induction sounder (EMS), and a ground-penetrating radar (GPR). The laser altimeter provides the distance to the snow or ice surface, whereas the induction sounder measures the distance from the sensor to the ice–water interface. Hence the snow-plus-ice thickness can be obtained (Prinsenberg et al., 2012). Comparisons with drill hole data showed that the ice thickness values derived from sounding agree well within ±0.1 m over flat homogeneous ice (Haas et al., 2006; Sim-

TCD
9, 5445–5483, 2015

ilä et al., 2010). The accuracy decreases over ridges and deformed ice; the maximum thickness can be underestimated by as much as 50 % in the worst cases (Haas et al., 2006; Similä et al., 2010). Snow thickness profiles were collected concurrently with a ground-penetrating radar (GPR) operating at a frequency of 1000 MHz. Using those snow thickness profiles, sea ice thickness could be estimated. All data are available on the DFO's Maritimes Website (http://www.bio.gc.ca/science/research-recherche/ocean/ice-glace/data-donnees-eng.php) including pictures, notes and reports of the survey.

4.2 Data sets and data processing

On 19 and 20 March 2011, four C-band Radarsat-2 quad-polarization images were acquired nearly coincident with the measurement. The Google Earth and Pauli RGB images of this data set are shown in Fig. 8. Important SAR parameters are listed in Table 3. The Radarsat-2 data are originally processed as single-look slant range complex (SSC) data in a scattering matrix format. With the quad-polarization data, the CTLR compact polarimetry mode can be generated via Eq. (3).

Eight EMS profiles were measured within the coverage of the four SAR images (Fig. 8). The time difference between the SAR acquisitions and EMS flights are summarized in Table 4. A direct comparison between SAR data and ice thickness may cause errors due to the time and resolution differences. The sampling rate for EMS and laser is 10 Hz, which, given typical helicopter survey speed of 80 mph, corresponds to a spatial sampling interval of about 3–4 m. While the footprint size of the laser is very small (several centimeters), the footprint of EM is around 20 m at a typical operation height of 5–6 m. For this experiment, the GPR was configured to a scan rate of approximately 30 scans per second. When flying at 60–80 knots, the ground sample spacing is approximately one sample per 1.0–1.5 m. In order to mitigate the errors caused by time and resolution differences, we developed the following processing chain for the SAR and in-situ data.

TCD
9, 5445–5483, 2015

1. Open water and land regions were masked, leaving only the ice-covered region for analysis.

2. The EMS ice thickness values below 0.1 cm were removed to consider the measurement accuracy of the EMS.

3. Deformed ice, ridge, and iceberg areas were removed using information in the reports, pictures and laser data that were collected along the survey lines.

4. The regions with GPR snow thickness values higher than 0.20 m were removed, because snow layers thinner than 0.20 m are nearly transparent to C-band radar waves, and the backscatter from the snow surface and volume can be neglected (Stiles and Ulaby, 1980; Nakamura et al., 2009).

5. For homogeneous ice areas ("homogenous" in the sense that there is only one ice type in the area) of at least 50 m in length, the snow thickness, snow-plus-ice thickness, surface roughness, and simulated CP SAR data were averaged along the flight transects. We used a 13 × 13 pixel window to average scattering parameters corresponding to a fixed length of 50 m on the ground.

6. Sea ice thickness was extracted from the averaged GRP snow depth and snow-plus-ice thickness values.

7. Finally we calculated CP-Ratio from Eq. (14) using the averaged complex backscattering coefficients.

This processing chain ensures that, only level ice is considered for which the EMS system delivers reliable thickness data with an acceptable accuracy. The total length of the profile segments that we used in this study amounts to about 10 km (702 samples). From the histograms shown in Fig. 9 we found, that the maximum ice thickness was 3.3 m, the mean ice thickness 0.91 m, and the modal thickness (peak) representing the ice thickness most frequently encountered 0.50 m.

TCD
9, 5445–5483, 2015

4.3 Ice thickness retrieval

To investigate the possibility of using the proposed polarimetric parameter CP-Ratio to estimate sea ice thickness from SAR images, we plotted ice thickness values obtained during the field campaign described above with corresponding values of CP-Ratio derived from the Radarsat-2 images (Fig. 10). It can be seen that at C-band, the CP-Ratio shows a negative trend relative to the ice thickness as the simulated results given in Sect. 3.2 predicted. As Fig. 10 reveals, the highest sensitivity occurs between 0 and 0.5 m and saturates with thickness values exceeding 2 m (corresponds to multi-year ice). The reason is that multi-year ice survived at least one melting season so that the salinity is very low and almost constant in the upper ice layer, which means that the dielectric constant does not change substantially either as a function of ice thickness.

We applied two different fits, a linear and a logarithmic one, to obtain an empirical relationship between the ice thickness and CP-Ratio. The best regression was obtained using a logarithmic function (Fig. 10), which can be described as:

$$\text{CP-Ratio} = 0.2014 - 0.06383\ln(H). \quad (14)$$

The RMS error and the correlation coefficients between ice thickness and CP-Ratio are 0.0511 and 0.784, respectively. This equation is obtained without considering the radar incidence angle (and can hence be applied without knowing it).

Since our data comprise different incidence angles (29, 42 and 49° at the survey positions), we can refine the relationships between ice-thickness and the CP-Ratio dependent on incidence angle (Fig. 11). We found that the level of CP-Ratio decreases as the incidence angle increases at a given value of the sea ice thickness. This observation compares well with the forward simulation studies as shown in Fig. 5. For Fig. 11, the empirical equations and correlation coefficients are

$$\begin{aligned}
&\text{CP-Ratio} = 0.1541 - 0.06549\ln(H) \text{ for } 29^\circ \text{ incident angle } (\text{CC} = 0.92)\\
&\text{CP-Ratio} = 0.2017 - 0.07844\ln(H) \text{ for } 42^\circ \text{ incident angle } (\text{CC} = 0.84)\\
&\text{CP-Ratio} = 0.2551 - 0.10563\ln(H) \text{ for } 49^\circ \text{ incident angle } (\text{CC} = 0.87). \quad (15)
\end{aligned}$$

TCD
9, 5445–5483, 2015

These high correlations enable us to derive reliable thickness information for smooth level ice from radar images. The ice thickness can be estimated using an exponential function, which can be described as follows:

$$H = \exp\left[\frac{a - (\text{CP-Ratio})}{b}\right] \tag{16}$$

where a and b are the coefficients of the exponential fit.

At the next stage, we focused on the Radarsat-2 image #2 (which has the same incidence angle of 42° as image #1) to validate our method, whereas image #1 was used to fit the model for estimating ice thickness. The resulting equation was applied to image #2 to retrieve ice thickness, which was compared with the thickness data from the field campaign. The coefficients a and b of the empirical fit generated from image #1 are 0.213 and 0.081 respectively. The fitted curve and validation results are presented in Fig. 12. The RMS error and the relative error between the observed and the estimated ice thickness were 8.05 cm and 19.95 % in the thickness range from 0.1–1.5 m.

5 Discussion and conclusion

This paper provides a first analysis of sea ice thickness retrieval using compact polarimetric SAR. We developed a new parameter that we call CP-Ratio to estimate the thickness of undeformed first-year level ice. Numerical model simulations showed that this parameter is sensitive to changes of the dielectric constant that are linked to the growth of sea ice. We developed empirical relationships for the retrieval of level ice thickness from CP-Ratios obtained from polarimetric Radarsat-2 images using measured thickness data from a field campaign conducted in the Labrador Sea in 2011. For the validation of our results we also employed Radarsat-2 images for which thickness values were available. The optimal regression between CP-Ratio and ice thickness was achieved with an exponential fit. The RMS error was 8.05 cm, and the relative

TCD
9, 5445–5483, 2015

error amounted to 19.55 %. This indicates that the proposed parameter is very useful for the retrieval of first-year level ice thickness.

Since the thickness of deformed ice is underestimated by the EMS measurements by as much as 50 or 60 % in the worst cases, we could only study the case of level ice. The capability of CP SAR to retrieve the thickness of deformed ice, which reveals a larger variation of large-scale roughness with respect to the sensor resolution, needs to be further discussed and studied.

Sea ice deformation that results in increased surface roughness is primarily caused by compression processes. Peterson et al. (2008) and Toyota et al. (2009) have shown that the large-scale surface roughness of deformed sea ice is closely linked to the ice thickness due to ridging and rafting. Toyota et al. (2009) indicates that it may be possible to estimate the thickness distribution for deformed ice using roughness properties as proxies. Related to this suggestion, we note that the correlation coefficient between Σ_H and Σ_V could be used as a candidate parameter for determining ice-thickness with large-scale roughness. According to the X-SPM model, the correlation coefficient between Σ_H and Σ_V can be expressed as:

$$\begin{aligned}\text{Correlation} &= \frac{\langle |\Sigma_H \Sigma_V^*| \rangle}{\langle |\Sigma_H||\Sigma_V| \rangle} \\ &= \frac{|c_2| \left| \langle (R_S - R_P)(R_S + R_P)^* \rangle_{|\theta_l} \right|}{\langle |R_S + R_P| \rangle_{|\theta_l} \sqrt{cc_2 + ss_2} \langle |R_S - R_P| \rangle_{|\theta_l}} \\ &= \left| 2 \left(\sqrt{\frac{\pi \sin^2\theta}{2\sigma^2}} \exp\left\{ \frac{\sin^2\theta}{2\sigma^2} \right\} \text{Erfc}\left\{ \sqrt{\frac{\sin^2\theta}{2\sigma^2}} \right\} \right) - 1 \right|. \end{aligned} \quad (17)$$

It is only dependent on the standard deviation of the surface slope σ and the incidence angle θ, and independent of the dielectric constant of the sea ice.

TCD
9, 5445–5483, 2015

Figure 13 shows that the magnitude of the correlation coefficient decreases as σ increases. Further investigation on this issue is needed both theoretically and in comparison to matching field data.

Although our tests are performed on a limited sample of images, our findings demonstrate that the compact polarimetric SAR has great potential for sea-ice thickness detection. The several planned Earth-observing satellite missions supporting compact polarimetry will provide the wide swath coverage necessary for operational sea ice monitoring. Hence our approach potentially provides a new operational tool for sea ice thickness measurements with a large areal coverage.

Acknowledgements. This study was supported by the National Nature Science Foundation of China under Grant 41 306 193, and the R&D Special Foundation for Public Welfare Industry (201 341 8025). This work was carried out as part of the Dragon-3 Programme (10 501) by the Ministry of Science and Technology of the P. R. China and the European Space Agency. The authors would like to thank the Canadian Space Agency (CSA) for providing the Radarsat-2 data, and they are vey thankful to the department of Fisheries and Oceans Canada for their support in providing valuable snow and sea ice field data.

References

Arcone, A., Gow, A. G., and McGrew, S.: Structure and dielectric properties at 4.8 and 9.5 GHz of saline ice, J. Geophys. Res., 91, 14281–14303, 1986.

Charbonneau, F. J., Brisco, B., Raney, R. K., McNairn, H., Liu, C., Vachon, P., Vachon, W., Shang, J., DeAbreu, R., Champagne, Merzouki, A., and Geldsetzer, T.: Compact polarimetry overview and applications assessment, Can. J. Remote Sens., 36, 298–315, 2010.

Cox, G. and Weeks, W.: Equations for determining the gas and brine volumes in sea-ice samples, J. Glaciol., 29, 306–316, 1983.

Cox, G. and Weeks, W.: Numerical simulations of the profile properties of undeformed first-year sea ice during the growth season, J. Geophys. Res., 93, 12449–12460, 1988.

Dabboor, M. and Geldsetzer, T.: Towards sea ice classification using simulated RADARSAT Constellation Mission compact polarimetric SAR imagery, Remote Sens. Environ., 140, 189–195, 2014.

TCD
9, 5445–5483, 2015

Denbina, M. and Collins, M. J.: Iceberg detection using compact polarimetric synthetic aperture radar, Atmos. Ocean, 50, 437–446, 2012.
Fukusako, S.: Thermophysical properties of ice, snow, and sea ice, Int. J. Thermophys., 11, 353–372, 1990.
Goebell, S.: Comparison of coincident snow-freeboard and sea ice thickness profiles derived from helicopter-borne laser altimetry and electromagnetic induction sounding, J. Geophys. Res., 116, C08018, doi:10.1029/2009JC006055, 2011.
Haas, C., Gerland, S., Eicken, H., and Miller, H.: Comparison of sea-ice thickness measurements under summer and winter conditions in the Arctic using a small electromagnetic induction device, Geophysics, 62, 749–757, 1997.
Haas, C., Hendricks, S., and Doble, M.: Comparison of the sea ice thickness distribution in the Lincoln Sea and adjacent Arctic Ocean in 2004 and 2005, Ann. Glaciol., 44, 247–252, 2006.
Hajnsek, I., Pottier, E., and Cloude, S. R.: Inversion of surface parameters from polarimetric SAR, IEEE T. Geosci. Remote, 41, 727–744, 2003.
Huntemann, M., Heygster, G., Kaleschke, L., Krumpen, T., Mäkynen, M., and Drusch, M.: Empirical sea ice thickness retrieval during the freeze-up period from SMOS high incident angle observations, The Cryosphere, 8, 439–451, doi:10.5194/tc-8-439-2014, 2014.
Iodice, A., Natale, A., and Riccio, D.: Retrieval of soil surface parameters via a olarimetric two-scale model, IEEE T. Geosci. Remote, 49, 2531–2547, 2011.
Iodice, A., Natale, A., and Riccio, D.: Polarimetric two-scale model for soil moisture retrieval via dual-Pol HH-VV SAR data, IEEE J. Sel. Top. Appl., 6, 1163–1171, 2013.
Ji, S. Y., Yue, Q. J., and Zhang, X.: Thermodynamic analysis during sea ice growth in the Liaodong Bay, Mar. Environ. Sci., 19, 35–39, 2000.
Kaleschke, L., Tian-Kunze, X., Maaß, N., Mäkynen, M., and Drusch, M.: Sea ice thickness retrieval from SMOS brightness temperatures during the Arctic freeze-up period, Geophys. Res. Lett., 39, 1–5, doi:10.1029/2012GL050916, 2012.
Kim, J. W., Kim, D. J., and Hwang, B. J.: Characterization of Arctic sea ice thickness using high-resolution spaceborne polarimetric SAR data, IEEE T. Geosci. Remote, 50, 13–22, 2012.
Kovacs, A.: Sea Ice, Part I.: Bulk Salinity versus Ice Floe Thickness, USA Cold Regions Research and Engineering Laboratory, CRREL Rep. 97, United States Army, Corps of Engineers, 1–16, 1996.

TCD
9, 5445–5483, 2015

Kwok, R., Cunningham, G. F., Wensnahan, M., Rigor, I., Zwally, H. J., and Yi, D.: Thinning and volume loss of the Arctic Ocean sea ice cover: 2003–2008, J. Geophys. Res., 114, C07005, doi:10.1029/2009JC005312, 2009.

Liu, M., Dai, Y., Zhang, J., Zhang, X., and Meng, J.: Characterization of level sea-ice thickness in the Labrador Sea using C-band polarimetric SAR data, in: IET International Radar Conference 2013, Xi'an, China, 296–296, 2013.

Maykut, G. A.: Energy exchange over young sea ice in the central Arctic, J. Geophys. Res., 83, 3646–3658, 1978.

Maykut, G. A.: Large-scale heat exchange and ice production in the central Arctic, J. Geophys. Res., 87, 7991–7984, 1982.

Monaco, F. D., Quattro, N. D., Iodic, A., and Natale, A.: Extended small perturbation method and retrieval of natural surface parameters, in: Proc. 6th Eur. Radar Conf., Rome, Italy, 537–540, 2009.

Nakamura, K., Wakabayashi, H., Naoki, K., Nishio, F., Moriyama, T., and Uratsuka, S.: Observation of sea-ice thickness in the sea of Okhotsk by using dual-frequency and fully polarimetric airborne SAR (Pi-SAR) data, IEEE T. Geosci. Remote, 43, 2460–2469, 2009.

Nghiem, S. V., Kwok, R., Yueh, S. H., and Drinkwater, M. R.: Polarimetric signatures of sea ice, theoretical model, J. Geophys. Res., 100, 13665–13679, 1995.

Nord, M. E., Ainsworth, T. L., Lee, J. S., and Stacy, N. J. S.: Comparison of compact polarimetric aperture radar modes, IEEE T. Geosci. Remote, 47, 174–188, 2009.

Panigrahi, R. K. and Mishra, A. K.: Comparison of hybrid-Pol with quad-Pol scheme based on polarimetric information content, Int. J. Remote Sens., 33, 3531–3541, 2012.

Peterson, I. K., Prinsenberg, S. J., and Holladay, J. S.: Observations of sea ice thickness, surface roughness and ice motion in Amundsen Gulf, J. Geophys. Res., 113, 1–14, 2008.

Prinsenberg, S. J., Peterson, I. K., Holladay, J. S., and Lalumiere, L.: Labrador shelf pack ice and iceberg survey, March 2011, Can. Tech. Rep. Hydrogr. Ocean Sci., 275, 1–44, 2012, http://www.ocean-sci.net/275/1/2012/.

Raney, R.: Hybrid polarity SAR architecture, IEEE T. Geosci. Remote, 45, 3397–3404, 2007.

Salberg, A. B., Rudjord, O., and Solberg, A. H. S.: Oil spill detection in hybrid-polarimetric SAR images, IEEE T. Geosci. Remote, 52, 6521–6533, 2014.

Similä, M., Mäkynen, M., and Heiler, I.: Comparison between C band synthetic aperture radar and 3-D laser scanner statistics for the Baltic Sea ice, J. Geophys. Res., 115, 1–18, doi:10.1029/2009JC005970, 2010.

TCD
9, 5445–5483, 2015

Soulis, E. D., Lennox, W. C., and Sykes, J. F.: Estimation of the thickness of undeformed first year ice using radar backscatter, in: Geoscience and Remote Sensing Symposium, IGARSS'89, 12th Canadian Symposium on Remote Sensing, Vancouver, Canada, 2366–2369, 1989.

Souyris, J. C., Imbo, P., Fjortoft, R., Mingot, S., and Lee, J. S.: Compact polarimetry based on symmetry properties of geophysical media: the $\pi/4$ mode, IEEE T. Geosci. Remote, 43, 634–646, 2005.

Stiles, W. H. and Ulaby, F. T.: The active and passive microwave response to snow parameters, J. Geophys. Res., 85, 1037–1044, 1980.

Toyota, T., Nakamura, K., Uto, S., Ohshima, K. I., and Ebuchi, N.: Retrieval of sea ice thickness distribution in the seasonal ice zone from airborne L-band SAR, Int. J. Remote Sens., 30, 3171–3189, 2009.

Ulaby, F. T., Moore, R. K., and Fung, A. K.: Microwave Remote Rensing: Active and Passive, vol. II, Addison-Wesley, Reading, MA, 1982.

Vancoppenolle, M., Fichefet, T., and Bitz, C. M.: On the sensitivity of undeformed Arctic sea ice to its vertical salinity profile, Geophys. Res. Lett., 32, L16502, doi:10.1029/2005GL023427, 2005.

Vant, M. R., Ramseier, R. O., and Makios, V.: The complex dielectric constant of sea ice at frequencies in the range 0.1 to 40 GHz, J. Appl. Phys., 49, 1264–1280, 1978.

Wadhams, P.: A comparison of sonar and laser profiles along corresponding tracks in the Arctic Ocean, in: Sea Ice Processes and Models, edited by: Pritchard, R. S., Univ. of Washington Press, Seattle, Wash., 283–299, 1980.

Wakabayashi, H., Matsuoka, T., and Nakamura, K.: Polarimetric characteristics of sea ice in the Sea of Okhotsk observed by airborne L-band SAR, IEEE T. Geosci. Remote, 42, 2412–2425, 2004.

Yue, Q. J., Ji, S. Y., Miao, W. D., and Wu, S. L.: Solar radiation on sea ice in Liaodong Bay, Oceanol. ET Limnol. Sin., 31, 562–567, 2000.

TCD
9, 5445–5483, 2015

Table 1. Equations and parameters used for the sea ice thermodynamic model.

Term	Equations	Parameters	Comments
The incident short wave radiation	$F_r = (1 - 0.0065C^2)Q_{so}a^m$	$a^m = 0.99 - 0.17\,m$	a^m is the atmospheric transmissivity;
	Ji et al. (2000);	$m = 0.83$	C is the cloud coverage;
	Yue et al. (2000)	C in the range $0 \sim 10$	Q_{so} is the solar irradiance for the Dth day in a year;
	$Q_{so} = Q_s(\sin\beta\sin\delta + \cos\beta\cos\delta\cos H)$	$Q_s = I_s(1 + 0.033\cos(2\pi D/365))$	I_s is the solar radiation constant (unit: $W\,m^{-2}$);
	Yue et al. (2000)	$\delta = 23.44^\circ\cos[(172 - d)2\pi/365]$ $Ha = 15(t - 12)\pi/180 + \lambda$	δ is the declination angle of the sun; Ha is the local solar hour angle; β and λ are the latitude and longitude; t is Universal Time Coordinated.
The long wave radiation	$F_E = \varepsilon_i\sigma T_0^4$	$\sigma = 5.670 \times 10^{-8}$	σ is the Stefan–Boltzman constant (unit: $w\,(m^{-2}\,K^{-4})$);
	Maykut (1978)	$\varepsilon_i = 0.97$	T_0 is the surface temperature of sea ice (unit: K);
	$F_L = (1 + kC^2)\varepsilon_a\sigma T_a^4$	$k = 0.0017$	T_a is the air temperature (unit: K);
	Maykut (1978)	$\varepsilon_a = 0.55 + d \times 0.052^{1/2}$ e is the water vapor pressure at T_a (unit: hPa).	ε_i is the emissivity of sea ice; ε_a is the emissivity of atmosphere;
The sensible heat flux	$F_s = \rho_a C_p C_s u(T_a - T_0)$	$\rho_a = 1.3$	ρ_a is the air density (unit: $kg\,m^{-3}$);
	Cox and Weeks (1988)	$C_p = 1006$	C_p is the specific heat at constant pressure (unit: $J\,(kg\,K)^{-1}$);
		$C_s = 0.003$	C_s is the sensible heat transfer coefficient; u is the wind speed
The latent heat flux	$F_e = \rho_a L C_e u(q_a - q_0)$ Cox and Weeks (1988)	$C_e = 0.00175$ $L = 2.5 \times 10^6 - 2.274 \times 10^3(T_a - 273.15)$	L is the latent heat of vaporization (unit: $J\,kg^{-1}$);
	$q_a - q_0 = \frac{0.622}{p_0}$	$p_0 = 1013$	p_0 is the surface atmospheric pressure (unit: mbar);
	$\begin{bmatrix} a(fT_a^4 - T_0^4) + b(fT_a^3 - T_0^3) + \\ c(fT_a^2 - T_0^2) + d(fT_a - T_0) + \\ e(f - 1) \end{bmatrix}$	$a = 2.7798202 \times 10^{-6}$;	f is the relative humidity;
	Cox and Weeks (1988)	$b = -2.6913393 \times 10^{-3}$; $c = 0.97920849$; $d = -158.63779$; $e = 9653.1925$;	a, b, c, d, and e are constants; a (unit: k^4), b (unit: k^3), c (unit: k^2), d (unit: k)
The albedo of sea ice	$\alpha = \beta_0 + \beta_1 H + \beta_2 H^2 + \beta_3 H^3$ Cox and Weeks (1988)	$\beta_0 = 0.2386$; $\beta_1 = 6.015 \times 10^{-3}$; $\beta_2 = -4.882 \times 10^{-5}$; $\beta_3 = 1.267 \times 10^{-7}$	H is the sea ice thickness (unit: cm).
The absorbed shortwave radiation	$I_0 = i_0(1 - \alpha)F_r$ Maykut (1978); Cox and Weeks (1988)	$i_0 = 17\,\%$	i_0 is the percent.
The upward conductive heat flux	$F_C = (k/H)(T_b - T_0)$ Cox and Weeks (1988)	$k = k_i(1 - V_b) + k_b f_{vb}$ $k_i = 4.17 \times 10^4[5.35 \times 10^{-3} - 2.568 \times 10^{-5}(T_0 - 273.15)]$ $k_b = 4.17 \times 10^4[1.25 \times 10^{-3} + 3.0 \times 10^{-5}(T_0 - 273.15) + 1.4 \times 10^{-7}(T_0 - 273.15)^2]$ $T_b = -1.8$	k, k_i, k_b are the conductivity of ice layer, pure ice and pure brine, respectively (unit: $W\,m^{-1}\,K^{-1}$); T_b is the freezing point (unit: °C); f_{vb} is volume fraction of sea ice brine inclusion.

TCD
9, 5445–5483, 2015

Table 2. Equations and parameters used for the sea ice properties parameters.

Term	Equations	Parameters	Comments
The ice thickness	$\frac{\Delta h}{\Delta t} = \frac{F_c(H)}{\rho L_i}$ (Cox and Weeks, 1988)	$L_f = 4.187 \times 10^3 (79.68 - 0.505$ $T_b - 0.0273 S_i) + 4.3115 S_i / T_b + 8 \times 10^{-4}$ $T_b S_i - 0.009 (T_b)^2$	$\Delta h / \Delta t$ is the sea ice growth rate when ice thickness is H (unit: $m s^{-1}$); ice thickness is the sum of ice growth rate.
	$H = \sum_{i=0}^{\text{Time}} \frac{\Delta h}{\Delta t} \Delta\text{Time}$	Fukusako (1990)	ΔTime is the time lag (unit: h).
The sea ice density and brine volume fraction	$\begin{cases} \rho = \frac{\rho_i F_1(T)}{F_1(T) - \rho_i S_i F_2(T)} \\ f_{vb} = \frac{\rho_i S_i}{F_1(T) - \rho_i S_i F_2(T)} \end{cases}$ Cox and Weeks (1983)	$\rho_i = 0.917 - 1.403 \times 10^{-4} T$	ρ is sea ice density (unit: $kg m^{-3}$); f_{vb} is the relative brine volume fraction ρ_i is pure ice density (unit: $kg m^{-3}$); T is the temperature of sea ice (unit: °C); T_a is the air temperature (unit: K); S_i is ice salinity.
The ice salinity	$\begin{cases} S_i = 14.24 - 19.39H \ (H \le 0.4m) \\ S_i = 7.88 - 1.59H \ (H > 0.4m) \end{cases}$ Cox and Weeks (1983)		H is the ice thickness (unit: m).
The permittivity of sea ice at C-band	$\varepsilon'_{\text{eff}} = 3.05 + 0.0072 f_{vb}$ $\varepsilon''_{\text{eff}} = 0.02 + 0.0033 f_{vb}$ Arcone et al. (1986); Vant et al., (1978)		f_{vb} is the relative brine volume fraction.

TCD
9, 5445–5483, 2015

Table 3. Specifications of Radarsat-2 SAR data.

Scene ID	Data/Time (UTC)	Polarization	Resolutions (m)	Incident angle (Deg.)	Beam Mode
#1	19 Mar 2011, 21:51	HH/VV/HV/VH (Quad)	8	42.0	FQ23
#2	19 Mar 2011, 21:51	HH/VV/HV/VH (Quad)	8	42.0	FQ23
#3	20 Mar 2011, 09:56	HH/VV/HV/VH (Quad)	8	49.0	FQ31
#4	19 Mar 2011, 10:25	HH/VV/HV/VH (Quad)	8	29.0	FQ9

TCD
9, 5445–5483, 2015

Table 4. Specifications of helicopter-borne EM ice thickness data sets.

EM ID	SAR data coincident with EM	Data/Time (UTC)	Time difference
P-1	#1	19 Mar 2011 14:47–15:00	~ 7 h
P-2	#1	19 Mar 2011 16:00–16:15	~ 5 h
P-3	#2	19 Mar 2011 16:15–16:30	~ 5 h
P-4	#3	20 Mar 2011 09:30–09:42	< 0.5 h
P-5	#3	20 Mar 2011 09:42–10:00	< 0.5 h
P-6	#4	19 Mar 2011 14:30–14:45	~ 4 h
P-7	#4	20 Mar 2012 12:00–12:15	~ 26 h
P-8	#4	20 Mar 2012 12:15–12:30	~ 26 h

TCD
9, 5445–5483, 2015

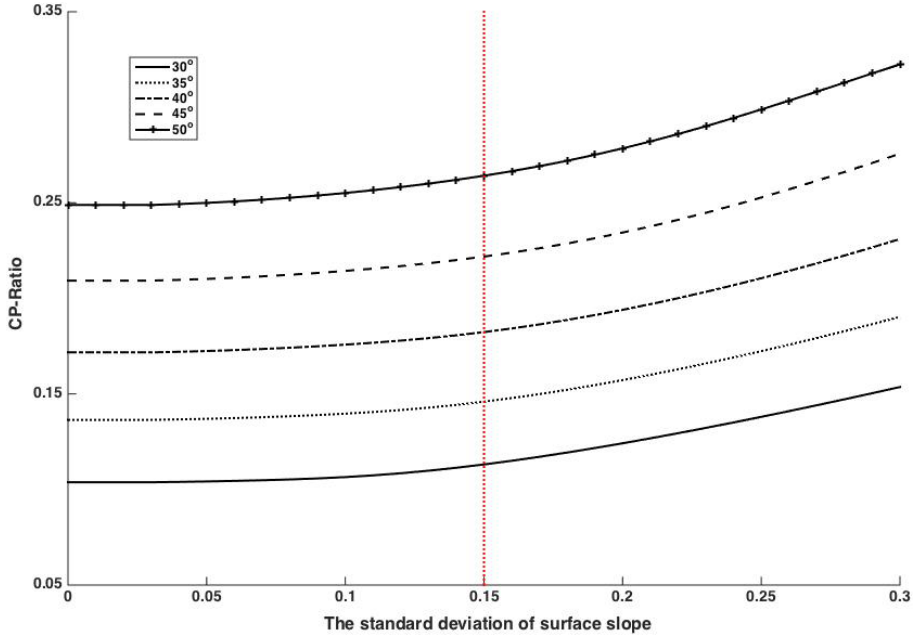

Figure 1. Variations of CP-Ratio as a function of the standard deviation of surface slope σ for different incidence angles and $\varepsilon = 3$. The red line marks the maximum threshold of σ for the validity of our approach.

TCD
9, 5445–5483, 2015

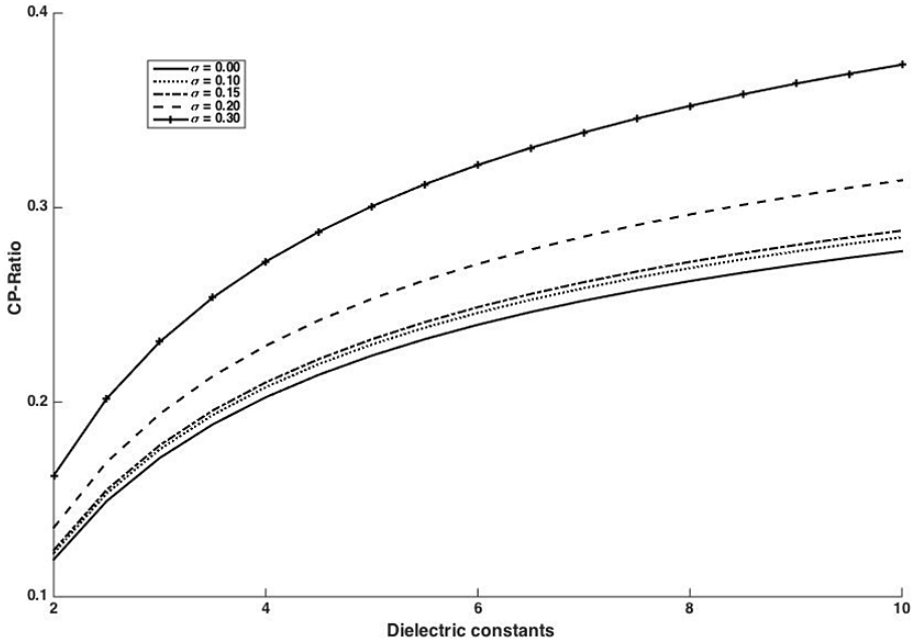

Figure 2. CP-Ratio as a function of dielectric constants for different σ and incidence angle = 30°.

TCD
9, 5445–5483, 2015

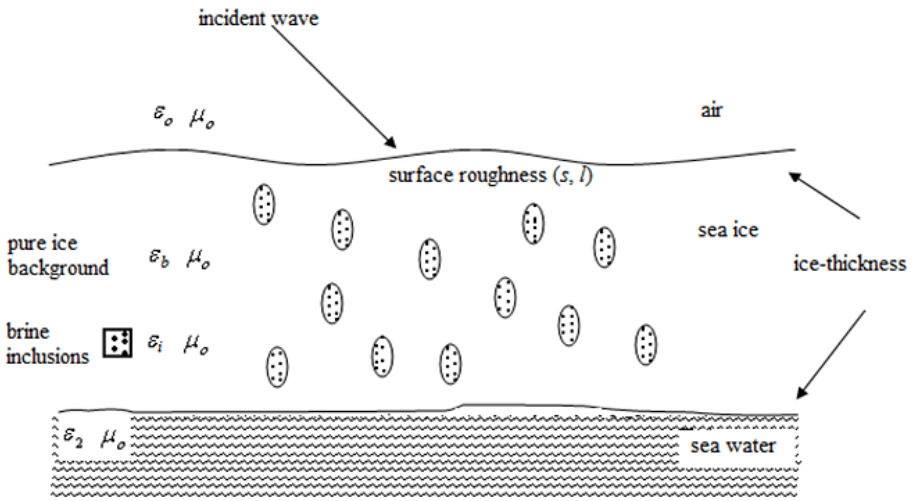

Figure 3. Structure and geometric model of the configuration of sea ice.

TCD
9, 5445–5483, 2015

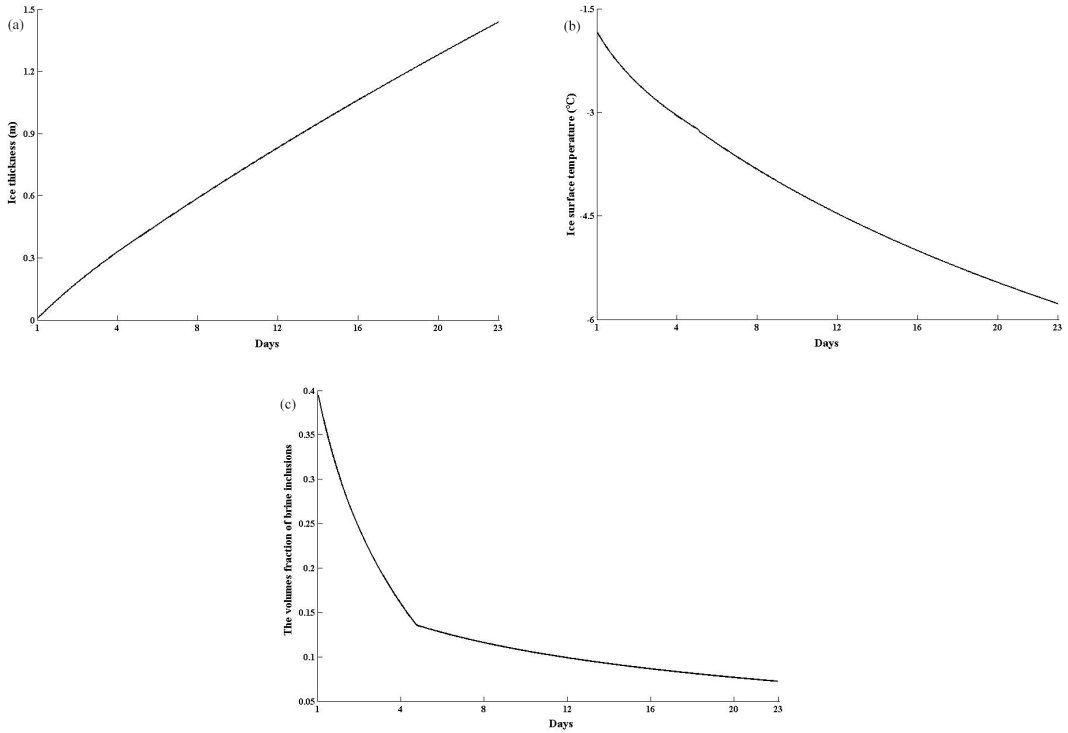

Figure 4. The simulated sea ice growth process **(a)** sea ice thickness, **(b)** sea ice temperature, **(c)** volume fraction of brine inclusions.

TCD
9, 5445–5483, 2015

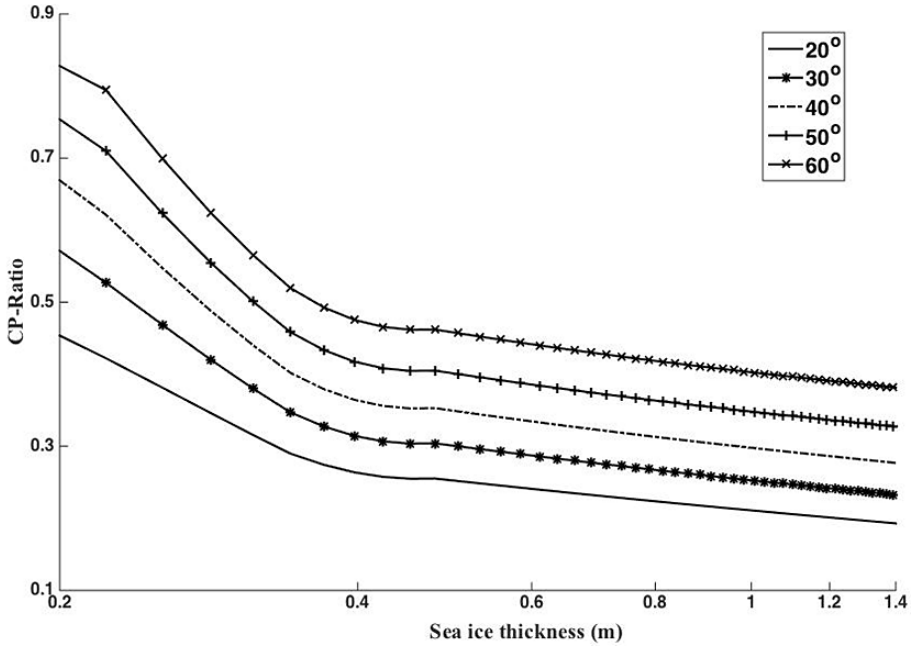

Figure 5. The relationship between CP-Ratio and ice thickness at different incidence angles for C-band radar (x axis in log scale). The incidence angle varies from 20 to 60°, and the input ice-surface roughness parameters are ks = 0.15, kl = 2.0, and σ = 0.1.

TCD
9, 5445–5483, 2015

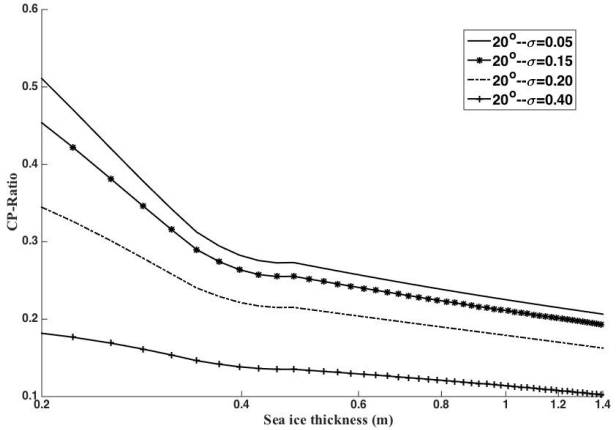

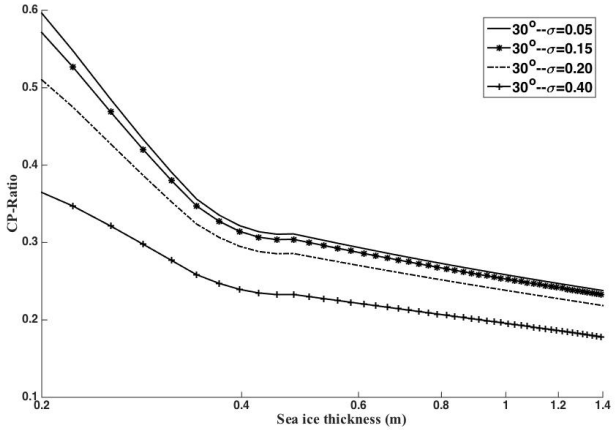

Figure 6. Slope sensitivity for Ratio (x axis in log scale). The standard deviation of the surface slope varies from 0.05 to 0.4, while ks = 0.15 and kl = 2.0. Top figure is for 20° incidence angle and bottom is for 30° incidence angle.

TCD
9, 5445–5483, 2015

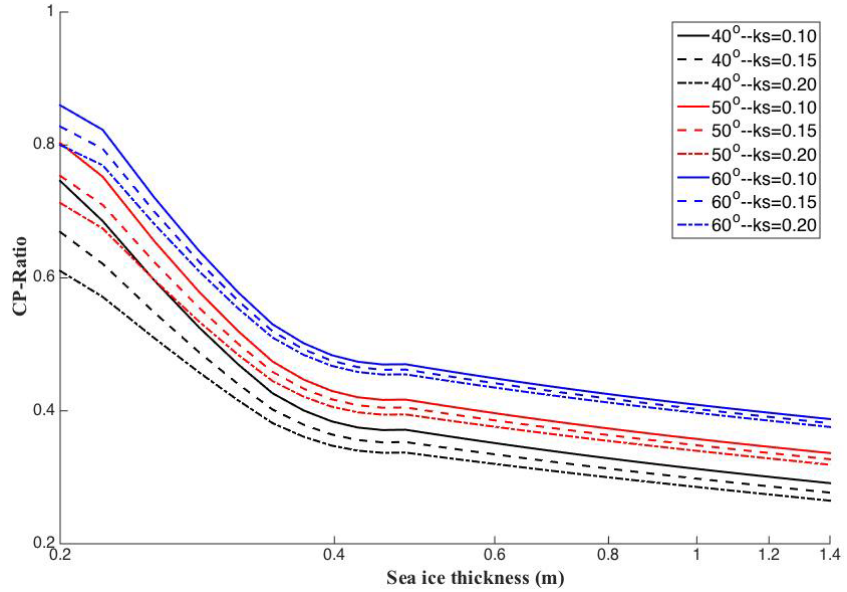

Figure 7. Small-scale roughness sensitivity for Ratio (x axis in log scale). The RMS height varies from 0.9 to 1.8 mm (ks = 0.1 ~ 0.2), while kl = 2.0 and σ = 0.1. Black color, red color, and blue color are for 40, 50, and 60° incidence angles.

TCD
9, 5445–5483, 2015

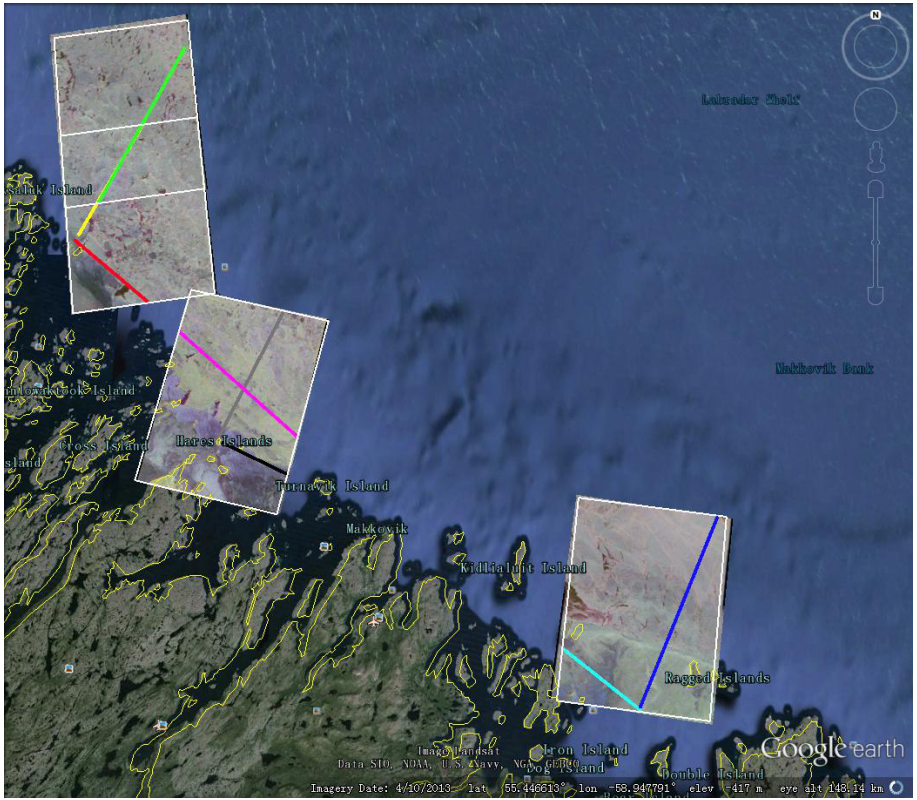

Figure 8. Location of the measurement site in the Labrador Sea, with four Pauli RGB decompositions of Radarsat-2 SAR images superimposed on the Google Earth© background. The lines overlaid on the SAR data are the induction sounder flight transects. Red: path-1 (P-1); yellow: path-2 (P-2); green: path-3 (P-3); cyan: path-4 (P-4); blue: path-5 (P-5); magenta: path-6 (P-6); black: path-7 (P-7); gray: path-8 (P-8).

TCD
9, 5445–5483, 2015

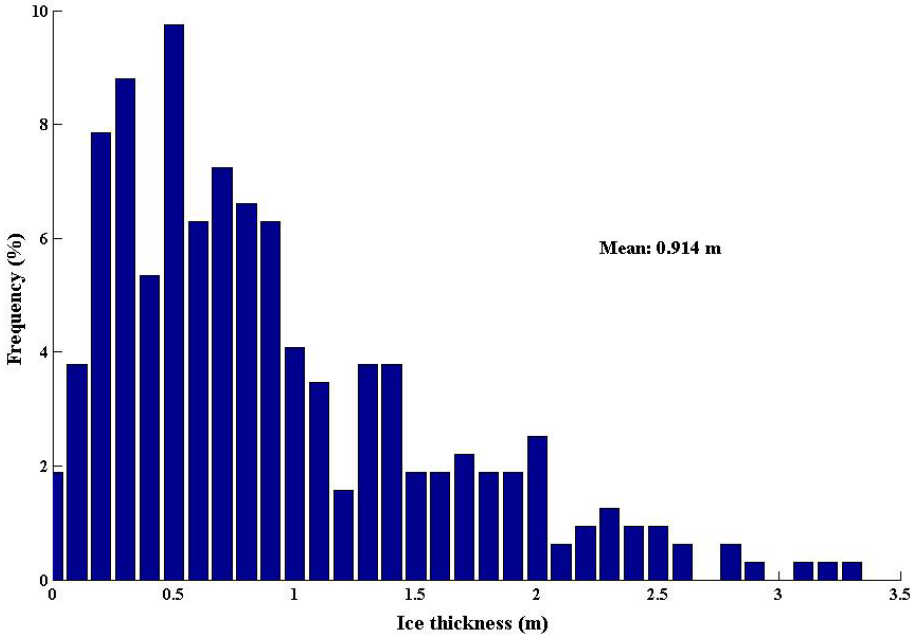

Figure 9. Histogram of averaged ice thickness in the Labrador Sea.

TCD
9, 5445–5483, 2015

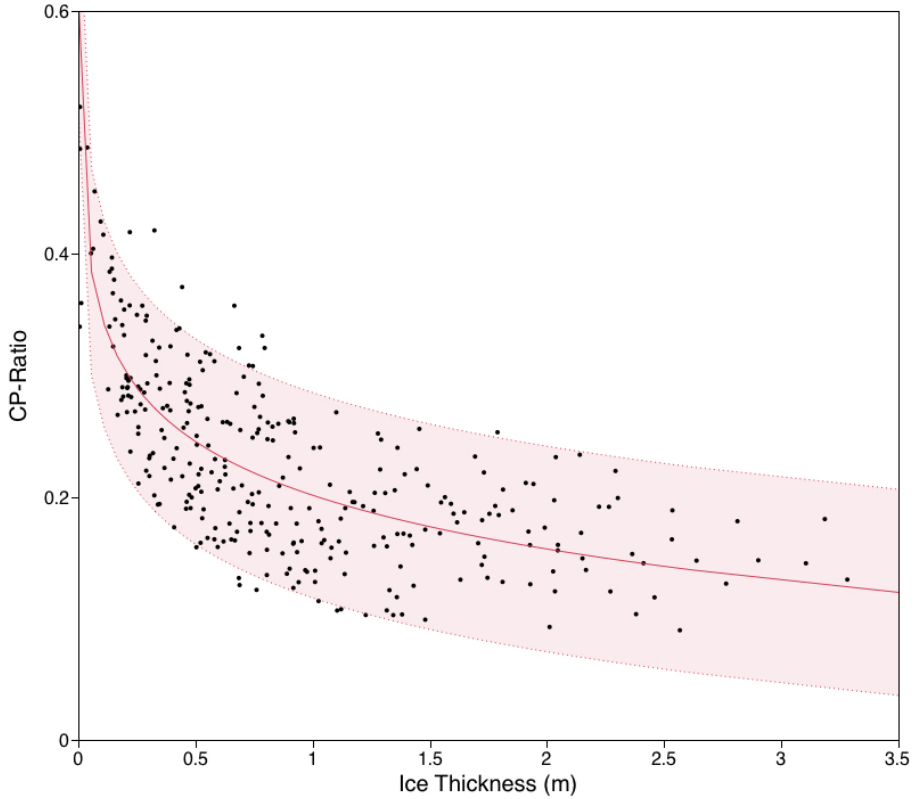

Figure 10. Regressions (solid lines) relating ice thickness to CP-Ratio. The dashed lines represent the 90 % confidence interval.

TCD
9, 5445–5483, 2015

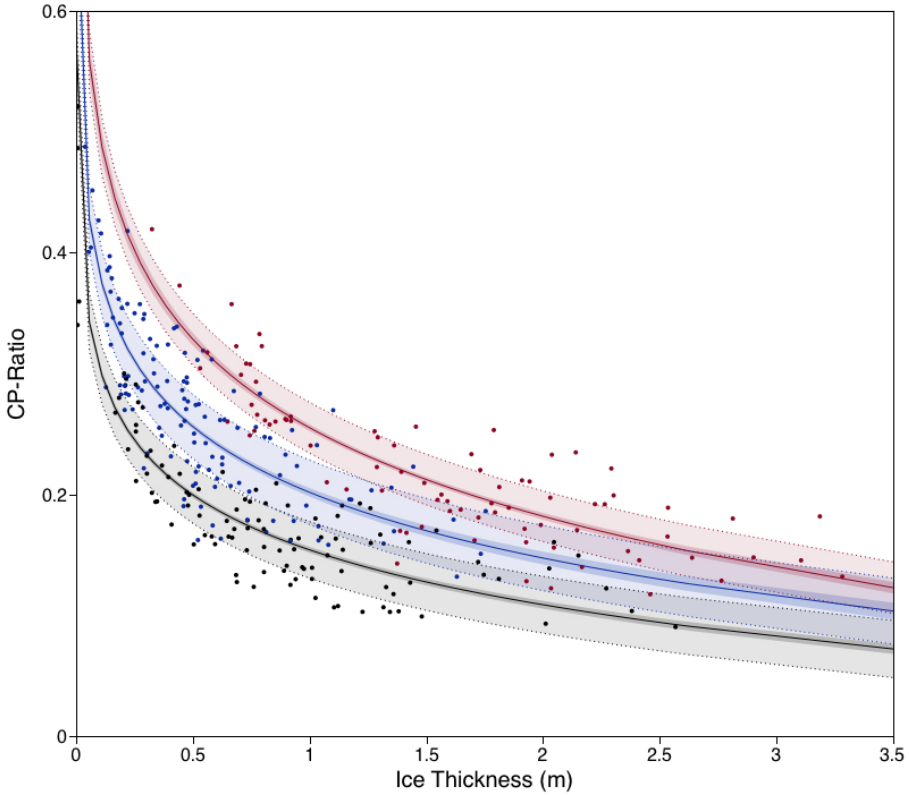

Figure 11. Regressions relating ice thickness to CP-Ratio at different incident angle. The solid lines represent the fit, dashed lines the 50 % confidence interval. The black, blue and red color is used for the incidence angle of 29, 42 and 49°, respectively.

TCD
9, 5445–5483, 2015

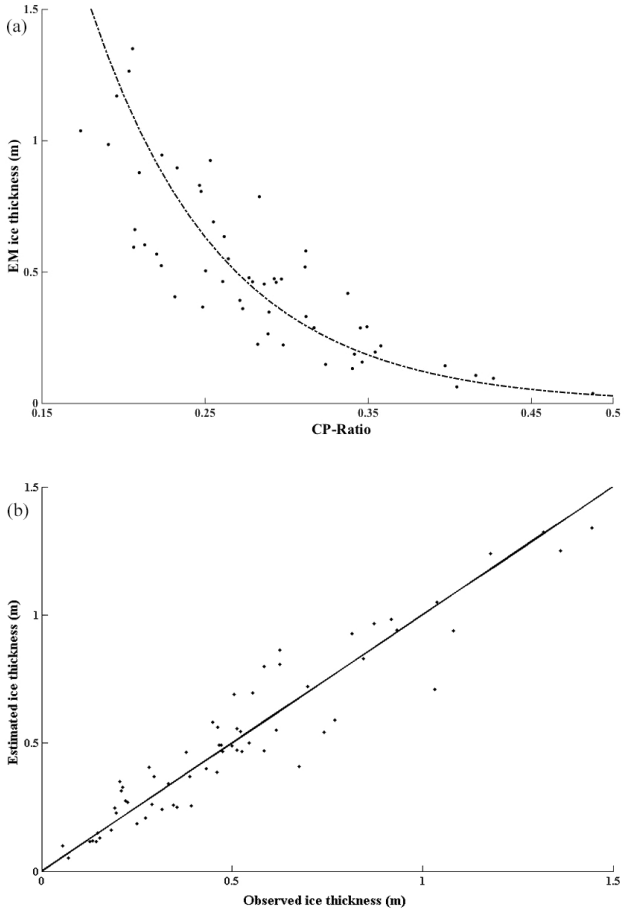

Figure 12. (a) Relationship between the CP-Ratio and the observed EM sea thickness. **(b)** Comparison between the observed and estimated ice thicknesses.

TCD
9, 5445–5483, 2015

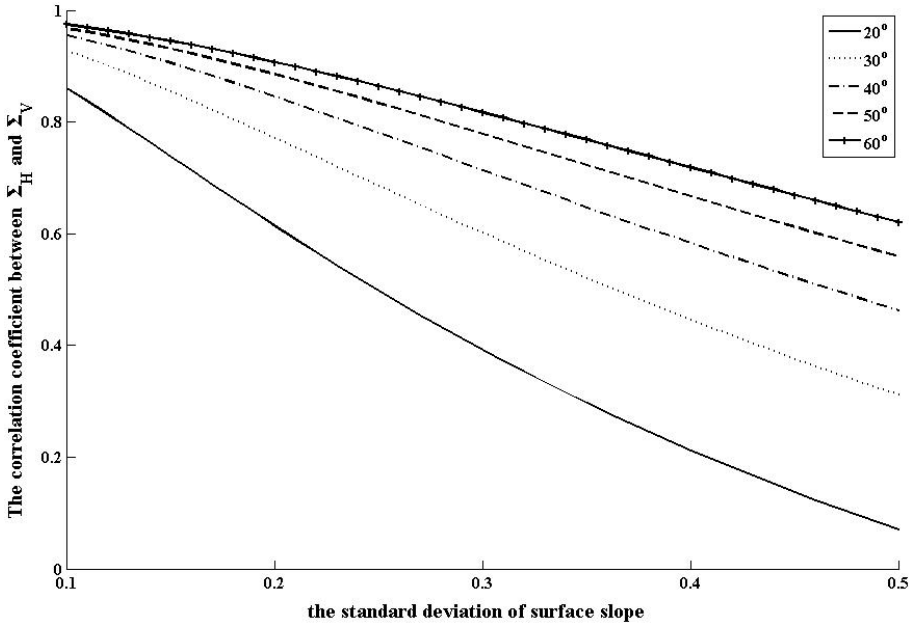

Figure 13. The correlation between Σ_H and Σ_V for different values of σ at different incidence angles.

TCD
9, 5445–5483, 2015